

First-principles calculation of oxygen vacancy effects on the magnetic properties of the perovskite SrNiO₃

Eunsoo Cho,¹ Konstantin Klyukin,¹ Shuai Ning ^{1,2} Jiarui Li ³ Riccardo Comin,³
Robert J. Green,^{4,5} Bilge Yildiz ^{1,6} and Caroline A. Ross ^{1,*}

¹Department of Materials Science and Engineering, Massachusetts Institute of Technology, Cambridge, Massachusetts 02139, USA

²School of Materials Science and Engineering, National Institute for Advanced Materials, Nankai University, Tianjin 300350, People's Republic of China

³Department of Physics, Massachusetts Institute of Technology, Cambridge, Massachusetts 02139, USA

⁴Department of Physics and Engineering Physics, University of Saskatchewan, Saskatoon, Saskatchewan, Canada S7N 5E2

⁵Stewart Blusson Quantum Matter Institute, University of British Columbia, Vancouver, British Columbia, Canada V6T 1Z4

⁶Department of Nuclear Science and Engineering, Massachusetts Institute of Technology, Cambridge, Massachusetts 02139, USA



(Received 14 March 2021; revised 7 July 2021; accepted 7 September 2021; published 27 September 2021)

Nickelates have been studied extensively due to their intriguing physical properties, but less attention has been paid to the properties of divalent *A*-site cation perovskite nickelates with a formal valence state of 4+ for Ni. Here, we study the electronic and magnetic properties of perovskite SrNiO_{3-δ} with an oxygen deficiency δ up to 0.375 using density functional theory. Because of the strong covalency and negative charge transfer energetics, the structure is predicted to exhibit ligand holes \underline{L} , with Ni present as $d^8\underline{L}^2$ or $d^7\underline{L}$ and significant magnetic moment at the oxygen sites. The ground state for $\delta = 0-0.375$ consists of ferromagnetically ordered Ni with the Ni and O moments coupled antiferromagnetically, and the removal of oxygen increases the net magnetization. These behaviors are also predicted for other *A*-site cations such as Ca and Ba. This work demonstrates the importance of ligand holes in oxides with formally high valence Ni, including their influence on the magnetic properties, and motivates further experimental study of the electronic and magnetic properties of nickelates with divalent *A*-site cations.

DOI: [10.1103/PhysRevMaterials.5.094413](https://doi.org/10.1103/PhysRevMaterials.5.094413)

I. INTRODUCTION

Nickelates exhibit distinct physical properties compared to oxides of lighter transition metals. The delicate interplay between structural distortions and the various energies (the charge transfer energy, Ni and O bandwidths, and Coulomb interaction U) leads to a range of complex and fascinating electronic behavior. Rare-earth perovskite nickelates, $R\text{NiO}_3$ are particularly well studied because the change in size of the *R* cation allows structural effects to be examined systematically [1,2]. The O $2p$ and Ni $3d$ bands are close in energy, ligand to metal charge transfer energies are small or negative, and the excitation with lowest energy is p - d electron transfer in which an electron moves from oxygen to the cation leaving a ligand hole \underline{L} [1–6]. The ground state includes a significant contribution from $d^{n+1}\underline{L}$ states hybridized with d^n states ($n = 7$ for Ni³⁺) and the materials are charge transfer insulators at low temperatures. Furthermore, perovskite $R\text{NiO}_3$ (except for $R = \text{La}$) are noncollinear antiferromagnetic insulators at low temperatures with a monoclinic distortion that produces two inequivalent Ni sites due to bond disproportionation [1,2,7]. Nickelates can exhibit metal-insulator transitions [8–10], charge disproportionation [11], charge localization [12], and superconductivity [13–16].

While rare-earth nickelates have been widely studied, fewer syntheses of alkaline-earth nickelates have been reported, and their electronic structure is not as well characterized. For a divalent *A* such as Ba²⁺ or Sr²⁺ and in the absence of oxygen vacancies, ANiO_3 would require a formal valence of Ni⁴⁺. There have been several studies of bulk hexagonal nickelates with divalent *A* such as SrNiO₃ [17,18] and BaNiO₃ [19–22]. Hexagonal SrNiO₃ has been synthesized by calcination [17] or by heating in 50–2000 atm oxygen (whereas 1 atm oxygen produced SrNiO_{2.5}) [18]. SrNiO_{2.5}, Sr₄Ni₃O₉, Sr₅Ni₄O₁₁, and Sr₉Ni₇O₂₁ [23–25] have also been synthesized. High valence Ni was proposed in Sr₄Ni₃O₉ [25] and in alkali metal nickelates such as a monoclinic Li₂NiO₃ [26,27] and KNiIO₆ [28,29]. Despite these works, the presence of Ni⁴⁺ in oxides remains controversial. Spectroscopic studies reveal considerable hybridization between Ni and O, the presence of O ligand holes, and Ni valence less than 4+ [22,26], analogous to the behavior found in the rare-earth nickelates.

The large ionic radii of divalent Sr and Ba lead to Goldschmidt tolerance factors exceeding 1, which explains the stability of the hexagonal SrNiO₃ and BaNiO₃ compounds compared to the cubic perovskite structure. However, cubic perovskite-structured compounds have been stabilized if there is only partial substitution of Ni, such as in cubic SrFe_{1-x}Ni_xO₃ with $x = 0-0.5$ [30,31]. Recently, a single unit cell layer of epitaxial cubic perovskite SrNiO₃ was stabilized by charge redistribution in a SrNiO₃/(LaFeO₃)_{*n*} superlattice

*caross@mit.edu

synthesized by molecular beam epitaxy [32], but another recent study to synthesize epitaxial cubic SrNiO₃ yielded phase separation into Sr₂NiO₃ and SrNi₂O₃ [33].

Further analysis of cubic perovskites A²⁺NiO₃ is motivated by the interesting electronic and magnetic properties reported to date. Half metallicity and ferromagnetism of perovskite SrNiO₃ was first predicted by *ab initio* simulations [34], where the ground state was ferromagnetic and the hybridization between d_{z^2} ($d_{x^2-y^2}$) and p_x (p_x and p_y) induces large magnetism at the O sites. Ni was proposed to be in the intermediate spin state of d^6 and the Ni-Ni interaction was explained by a double-exchange mechanism. A first principles study of hexagonal SrNiO₃ also predicts robust half-metallic properties and ferromagnetism, governed by the semicovaleant bonding between Ni and O [35]. Ni was predicted to induce ferromagnetism in antiferromagnetic SrFeO₃ [36,37], and experimentally SrFe_{1-x}Ni_xO₃ shows room temperature magnetism when $x \geq 0.4$ [30].

Here, we investigate the electronic and magnetic properties of the cubic perovskite SrNiO_{3- δ} (SNO) with $\delta = 0, 0.125, 0.250,$ and 0.375 through density functional theory (DFT) modeling. We focus on clarifying the electronic and magnetic configuration of Ni and the role of oxygen vacancies and strain on the electronic structure. Density of states (DOS) and projected density of states (PDOS) reveal the presence of oxygen ligand holes instead of tetravalent Ni. There is ferromagnetic coupling between the Ni cations, and significant magnetism originating from the O antiparallel to that of the Ni. This observation is maintained throughout increasing δ . Moreover, these behaviors extend to other A²⁺NiO₃ compounds including CaNiO₃ and BaNiO₃.

II. COMPUTATIONAL METHODS

All first principles calculations were performed with the Vienna Ab-initio Simulation Package (VASP). The Perdew-Burke-Ernzerhof (PBE) functional, a widely used type of generalized gradient approximation (GGA), was used within the calculation. The valence configurations used were Sr ($4s^2 4p^6 5s^2$), Ni ($4s^2 3d^8$), and O ($2s^2 2p^4$). The GGA+ U method was used to account for the Coulomb interaction of the Ni 3d electrons, with a specific U value of 6.2 eV ($U = 6.5$ eV, $J = 0.3$ eV), where the effective $U = 6.2$ eV was obtained for NiO using the simplified rotationally invariant method [38]. The energy cutoff used for cell relaxation and comparison of different symmetry was 600 eV, and for ionic relaxation the cutoff was 500 eV. k -point grids were maintained to a Monkhorst-Pack [39] $6 \times 6 \times 6$ mesh for all cubic structure calculations. We started from a $2 \times 2 \times 2$ cubic supercell consisting of 8 Sr, 8 Ni, and 24 O atoms, which is the smallest cell size that can take account of all ferromagnetic and antiferromagnetic ordering configurations. One, two, or three oxygen atoms were removed from the $2 \times 2 \times 2$ supercell to make a formula unit (f.u.) of SrNiO_{2.875} ($\delta = 0.125$), SrNiO_{2.75} ($\delta = 0.250$), or SrNiO_{2.675} ($\delta = 0.375$), respectively. For hexagonal (BaNiO₃-like 2H [40] and SrMnO₃-like 4H [41], both $P6_3/mmc$), rhombohedral ($R\bar{3}c$ and $R\bar{3}m$), and orthorhombic ($Pnma$) structures, a unit cell containing 2, 4, 8, 8, and 8 f.u. with $8 \times 8 \times 8$, $8 \times 8 \times 6$, $2 \times 2 \times 6$, $4 \times 4 \times 4$, and $6 \times 6 \times 4$ k -point grids were used, respectively. Structural

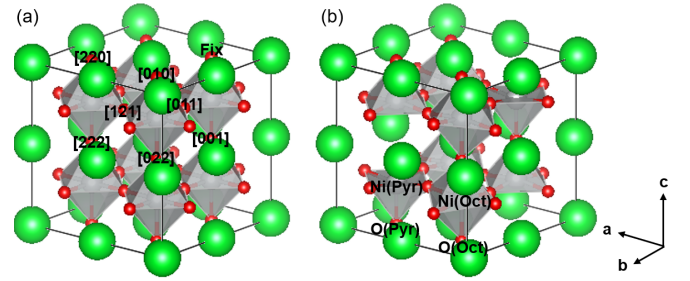


FIG. 1. (a) Crystal structure of SrNiO₃. Green, grey, and red correspond to Sr, Ni, and O atoms. One fixed V_O location (marked Fix) and the other seven possible positions for $\delta = 0.250$ are labeled. (b) Structure of [222] SNO_{2.75} with selected atoms for Figs. 2(c) and 2(d), and Table II labeled.

characterization was performed using VESTA [42] and Bader charge analysis was performed to determine the oxidation state of each atom [43]. The oxygen vacancy formation energy was determined using the following relations:

$$\Delta E(\text{first } V_O) = E(\text{one } V_O) - E(\text{nondefective}) + \frac{1}{2}E(O_2),$$

$$\Delta E(\text{second } V_O) = E(\text{two } V_O) - E(\text{one } V_O) + \frac{1}{2}E(O_2),$$

$$\Delta E(\text{third } V_O) = E(\text{three } V_O) - E(\text{two } V_O) + \frac{1}{2}E(O_2),$$

where the overbinding of the oxygen molecule was corrected in $E(O_2)$ [44]. We also used the Heyd-Scuseria-Ernzerhof (HSE) functional for nondefective and one-vacancy ferromagnetic SNO to demonstrate that the electronic and magnetic behavior are qualitatively the same as the PBE result (see Supplemental Material Fig. S1 [45]). We use the notation that majority carriers are spin up and minority carriers are spin down.

We applied in-plane strain to the $\delta = 0$ system to predict the effect of epitaxial growth on different substrates. The zero-strain lattice parameter was determined first from the fully relaxed structure. Up to +2% (−2%) of in-plane biaxial tensile (compressive) strain was applied by fixing the lattice in the x and y direction, while it was allowed to fully relax in the z direction. Moreover, we performed an analogous set of calculations with CaNiO₃ (CNO) and BaNiO₃ (BNO) to investigate the effect of the A cation and discuss the generality of the behavior of Ni and O. The valence configurations used for Ca and Ba are $3p^6 4s^2$ and $5s^2 5p^6 6s^2$, respectively.

III. RESULTS AND DISCUSSION

A. Structure, electronic properties, and magnetic ordering of SrNiO₃

We start by determining the most stable magnetic ordering of the cubic perovskite SrNiO₃ [Fig. 1(a)]. Four different types of ordering were initialized: ferromagnetic (FM), G -type antiferromagnetic (G -AFM, which has AFM order on both the xy plane (“in plane”) and xz or yz planes (“out of plane”), A -type antiferromagnetic (A -AFM, FM order in plane and AFM order out of plane), and C -type antiferromagnetic (C -AFM, AFM order in plane and FM order out of plane). FM was the ground state, followed by A -AFM, C -AFM, and G -AFM (Supplemental Material Table S1 [45]). The order of

stability is consistent with a prior report [34], considering the fact that the $U-J = 6.2$ eV used here is in between the 6 and 7 eV used in [34]. Structural relaxation indicated that atomic position symmetry was maintained for all types of ordering, so the octahedra did not exhibit distortions, which is attributed to the larger ionic radius of Sr^{2+} (118 pm) compared to that of rare-earth ions ($\text{La}^{3+} - \text{Lu}^{3+}$ have radii 102–86 pm). Calculations using a larger supercell or lowering the symmetry with an initial ion displacement yielded Ni-O-Ni bond angles of 180° and octahedral distortion was absent. This excludes the possibilities of noncollinear magnetization, bond disproportionation, or the E , S , or T -type antiferromagnetic orderings found in rare-earth nickelates [46–48].

FM and G -AFM SNO remained cubic, but A -AFM and C -AFM SNO had tetragonally distorted unit cells. The ground state cubic FM had a lattice parameter of 3.890 Å. We compared the energy of hexagonal, rhombohedral, and orthorhombic FM SNO relative to that of cubic SNO. Whereas 2H hexagonal is the most stable structure (-397.96 meV/f.u.), consistent with the experimental observations of hexagonal SNO, the rhombohedral or octahedral symmetry converged into the cubic. In particular, $Pnma$ and $R\bar{3}c$ structures which started with the presence of octahedral tilts converged into a cubic structure without rotations. This further suggests that other types of octahedral distortion or symmetry breaking are not stable. It is worth noting that the hexagonal structure used in [35] is a 4H structure, which is 349.13 meV/f.u. higher in energy than the 2H structure used in this study. The two different structures are visualized in Supplemental Material Fig. S2 [45]. The 2H structure is what was observed experimentally [18].

As reported in a previous study [34], $\delta = 0$ SNO is half metallic and the DOS at the Fermi level (E_F) arises from O $2p$ orbital electrons [see Fig. 2(a) and Supplemental Material Fig. S3 [45]]. In order to explain the electronic structure of SNO, we first focus on the PDOS of Ni. The e_g electrons show significant spin polarization, whereas the polarization of t_{2g} electrons is weak. The bonding-antibonding splitting of π bonds is 4 eV, which is smaller than that of the σ bonds which is around 8 eV, and this value is similar to the splitting of Co observed in SrCoO_3 [49]. The σ bonding can be represented as the occupied spin up electrons of Ni e_g hybridizing with O p_z at 6 eV below E_F . Between O p_x (p_y) orbitals and Ni d_{xz} (d_{yz}) orbitals, there are π bonding and antibonding hybridizations near 1 and 5 eV below E_F . In the PDOS of O, p orbitals with π bonding are less spin polarized, whereas those with σ bonding exhibit polarization.

The DOS exhibits the characteristics of oxygen ligand holes \bar{L} , where O p orbitals are partially filled and contribute to the metallic character. The presence of ligand holes is further supported by the qualitative similarity in PDOS calculated using the HSE functional, which also suggests the validity of $U-J = 6.2$ eV used in this study (Supplemental Material Fig. S1 [45]). The presence of ligand holes is analogous to findings in $R\text{NiO}_3$ [9,50–53] where Ni has a $d^8\bar{L}$ configuration, although in the case of SNO, we do not observe metal-insulator transitions upon introducing oxygen vacancies (discussed in Sec. III B) as seen in SmNiO_3 or NdNiO_3 [9,10]. The presence of ligand holes was also suggested in other ABO_3 compounds with divalent A such as SrCoO_3 or CaFeO_3 [49,54], and the

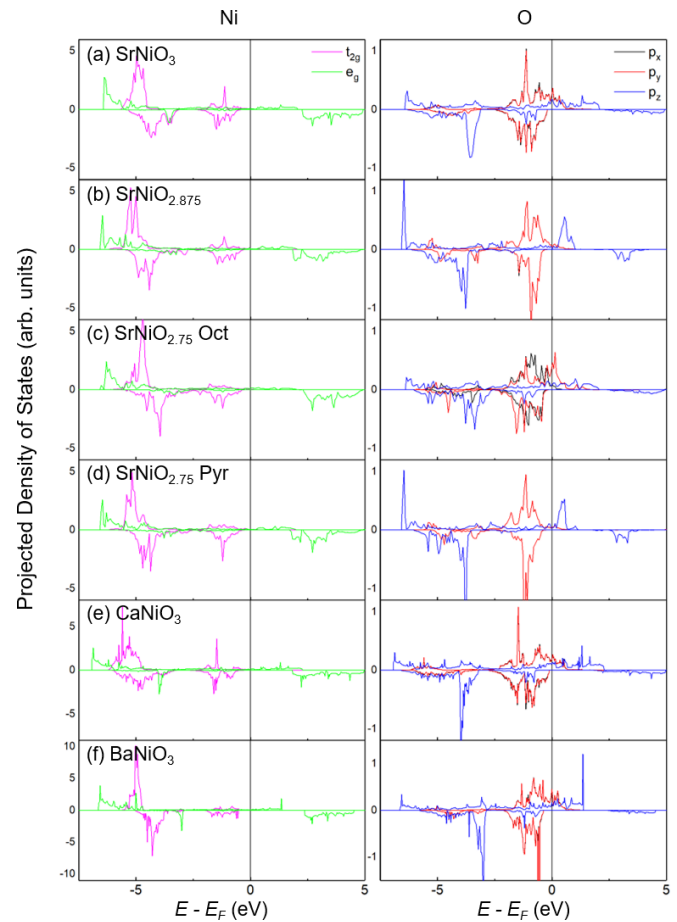


FIG. 2. PDOS of Ni and O bonded along the c axis of Ni in FM SNO, when (a) $\delta = 0$, (b) $\delta = 0.125$, (c) octahedrally coordinated $\delta = 0.250$, (d) pyramid coordinated $\delta = 0.250$, (e) CaNiO_3 , and (f) BaNiO_3 . Because the selected O is bonded in the z direction, the p_z orbital participates in σ bonding, and p_x and p_y orbitals participate in π bonding. In (a), (b), (d), (e), (f) O, the p_x and p_y PDOS overlap.

electronic structure observed here has similarities to those. However, Ni has a negligible contribution to the metallicity unlike SrFeO_3 or SrCoO_3 where Fe, Co, and O all contribute to states near the Fermi level [55].

Based on these PDOS, we propose an electronic configuration (Fig. 3) where Ni has all six t_{2g} electrons and two spin-up electrons in e_g , and for O, p_x and p_y are filled but only a spin-down electron occupies p_z . This configuration is further supported by noting that the Ni PDOS is similar to that calculated for SmNiO_3 (GGA+ U) [56] where Ni would have a formal charge of 3+, d^7 , but with a contribution of $d^8\bar{L}$, as well as being similar to that of NiO (GGA+ U) [57] and

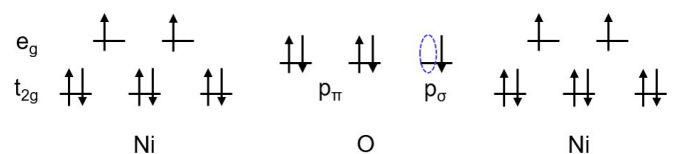


FIG. 3. Schematic of the proposed electronic structure of Ni and O in SNO, with the dashed circle indicating the ligand hole in O.

TABLE I. Bader charge analysis results of SNO_3 , $\text{SNO}_{2.875}$, and [222] $\text{SNO}_{2.75}$. Oxygen charge and magnetic moments (μ) are averaged over the supercell.

	Sr		O-Ni-O		O-Ni- V_O		O	
	Charge	μ (μ_B)	Charge	μ (μ_B)	Charge	μ (μ_B)	Charge	μ (μ_B)
SrNiO_3	+1.630	0.015	+1.414	1.330			-1.015	-0.451
$\text{SrNiO}_{2.875}$	+1.594	0.013	+1.423	1.363	+1.261	1.310	-1.037	-0.391
[222] $\text{SrNiO}_{2.75}$	+1.596	0.011	+1.388	1.448	+1.226	1.330	-1.055	-0.330

Li-doped NiO (GGA+ U and HSE) [58] where Ni should be in the 2+ oxidation state, d^8 . We have integrated the area of the PDOS below E_F to estimate the ratio of electrons between the e_g and t_{2g} orbitals, which shows that the area of e_g is around one-third of t_{2g} (Supplemental Material Table S2 [45]). These results imply that the electronic characteristics of Ni in SNO are close to $d^8\bar{L}^2$ or a mixture of $d^7\bar{L}$ and $d^8\bar{L}^2$. The $d^8\bar{L}^2$ -like configuration can also explain how the FM ordering of ground state SNO can be observed, because the spin-up electron from either Ni e_g orbital adjacent to O can hop to the O p_z orbital. In other words, the coupling of the magnetic moments is FM between Ni-Ni, FM between O-O, and AFM between Ni-O. This is also consistent with the sign of the magnetic moment of Ni and O, which are $1.343 \mu_B$ and $-0.395 \mu_B$ respectively. One interesting observation is that even though Ni orders ferromagnetically with a nonzero moment, the net magnetization of the system is nearly zero because the oxygens have an average magnetic moment about one-third that of Ni. Such half metallicity and magnetic ordering of SNO would have interesting consequences in tunnel magnetoresistance, x-ray magnetic circular dichroism, or neutron diffraction experiments.

The results are consistent with a $d^8\bar{L}^2$ -like configuration of Ni rather than the d^6 of Ni with a nominal valence state of 4+. However, we expect the electron not to be localized at a specific site, but to be delocalized due to the covalency of the bonds. Bader charge analysis (Table I) was performed to help clarify the electronic state of O. Oxygen has a charge of -1 , instead of -2 expected when the bonding is fully ionic, also supporting the presence of a ligand hole in O. Such covalent bonding and strong hybridization of Ni $3d$ and O $2p$ is commonly observed in RNiO_3 through x-ray absorption spectroscopy [59]. The covalency between Ni and O is also reported in NdNiO_3 , as the oxygen contribution in the electronic states is appreciable [60]. Prior DFT work on SNO [34,35] did not discuss oxygen ligand holes, but showed that perovskite SNO and 4H-SNO have similar electronic and magnetic properties.

We selected FM SNO, the ground state ordering, to apply epitaxial strain in the (001) plane, distorting the cubic structure into tetragonal. The magnitude of both Ni and O moments increases as tensile strain is applied, but the total magnetization remains nearly zero for all strain states because of the AFM coupling between Ni and O (Fig. 4). The increase in the Ni moment with strain is analogous to an experimental finding in $\text{SrCoO}_{3-\delta}$, where the Co valence state increased as epitaxial films were grown on substrates with larger lattice parameters, observed from the increase in oxygen deficiency [61]. Applying strain in both (001) and (111) orientations of bulk SNO did not stabilize the cubic structure over the

hexagonal structure. However, when two layers of (111) cubic SNO are sandwiched in between (111) cubic SrTiO_3 , the energy is more than 2 eV lower than that of two layers of (0001) 2H hexagonal SNO sandwiched within SrTiO_3 . Moreover, the magnetic moments of the Ni in the stabilized (111) SNO layer were $1.414 \mu_B$, and the electronic structure was similar to the bulk result (Supplemental Material Fig. S4 [45]), suggesting strategies for realizing cubic SNO within a heterostructure.

B. Oxygen vacancy effects in $\text{SNO}_{2.875}$ ($\delta = 0.125$), $\text{SNO}_{2.75}$ ($\delta = 0.250$), and $\text{SNO}_{2.625}$ ($\delta = 0.375$)

The behavior of perovskites is dramatically affected by oxygen vacancies (V_O), which lower the valence state of the cations, affect the number and mobility of charge carriers, and lead to structural distortions [62]. Structural effects can include a change in the crystal structure from perovskite to brownmillerite, $\text{ABO}_{2.5}$, on removal of sufficient oxygen [63,64]. The effects of V_O have been extensively studied for $\text{ABO}_{3-\delta}$ cobaltates, ferrites, and manganates with $A = \text{Sr, Ba}$ and $B = \text{Mn, Fe, and Co}$ [49,65–72]. The formation energy of V_O decreased as the radius of the B site cation decreased, but the magnetism was not analyzed in detail [73–75]. V_O interactions were studied in $\text{SrFeO}_{3-\delta}$, and V_O formation and transport were investigated in $(\text{La, Sr})\text{FeO}_{3-\delta}$ and $(\text{Ba, Sr})(\text{Fe, Co})\text{O}_{3-\delta}$ [71,72,76,77]. Magnetic exchange interactions and Curie temperature were calculated for $\text{SrCoO}_{3-\delta}$ with $\delta \leq 0.15$ [66]. The magnetization

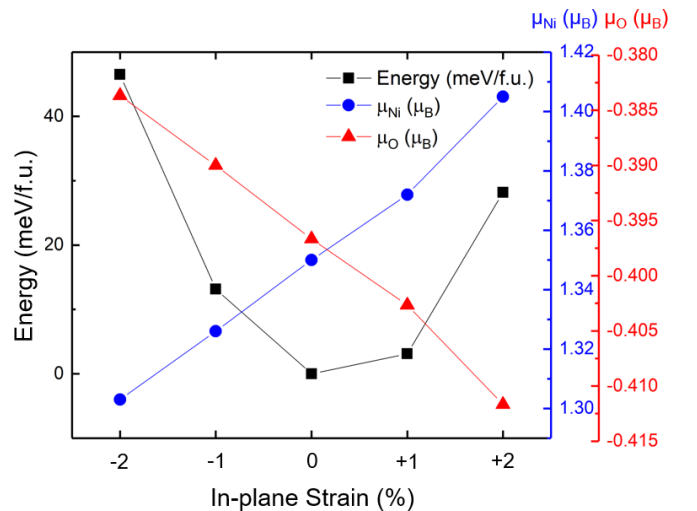


FIG. 4. Strain effects on cubic FM SrNiO_3 , showing the total energy and the magnetic moment of Ni and O as functions of the in-plane biaxial strain on the (001) plane.

of $\text{Sr}_{0.67}\text{La}_{0.33}\text{CoO}_{3-\delta}$ drops drastically at $\delta = 0.25$ because of the change in coupling [78]. V_O may be expected to occur readily in $A^{2+}\text{NiO}_3$ perovskites, but DFT studies in SNO [34,35] have not addressed their effects.

We investigated the structure and electronic properties of $\text{SrNiO}_{2.875}$ ($\delta = 0.125$) by introducing one O vacancy in a $2 \times 2 \times 2$ SNO supercell. Considering all four types of magnetic ordering, we considered six nonequivalent locations where the vacancy can be placed. For FM and *G*-AFM, the vacancy was placed in a site connecting octahedra along the *c* axis of the crystal. Putting the vacancy along the *a* axis for FM does not yield qualitatively different results. However, for *A*-AFM and *C*-AFM, there are two possible cases which are the vacancy being located between Ni with the same spins (case 1) or opposite spins (case 2), and we considered both. Even with one O vacancy, FM was still the most stable ordering (Supplemental Material Table S1 [45]). The lattice of FM $\text{SNO}_{2.875}$ expanded in the direction where the vacancy was located as a consequence of the increase in the distance between the Ni cations adjacent to the vacancy, and octahedral tilts due to the vacancy were observed. The formation energy of one neutral oxygen vacancy per 8 f.u. is 0.34 eV for FM SNO. This is lower than other perovskites such as SrTiO_3 [79] or SrFeO_3 [76], and similar to that of SrNiO_3 reported in [73].

In the FM state of $\text{SrNiO}_{2.875}$ the total magnetization increased to $0.240 \mu_B/\text{f.u.}$ For Ni, the average moment increased to $1.356 \mu_B$, and for O, the magnitude of the average moment decreased to $-0.342 \mu_B$. The increase in net moment/f.u. is primarily due to the removal of one O atom and its moment; the change in the Ni contribution is only $0.013 \mu_B$ out of $0.240 \mu_B$. To further investigate how the oxygen vacancy affects the magnetism in FM $\text{SNO}_{2.875}$, we compared the PDOS of Ni and O along the Ni-O-Ni- V_O -Ni direction with that of the nondefective perovskite SNO ($\delta = 0$). Comparing the PDOS in Fig. 2(b) with Fig. 2(a), a more hole like feature in O p_z appears near the peak just above E_F , because the absence of O in the other direction prohibits further exchange, and as a consequence, the σ bonding and the delocalization of the spin-up electron is weakened. In contrast, equatorial oxygens that do not have broken Ni-O bonds have qualitatively the same PDOS properties as those of SrNiO_3 (Supplemental Material Fig. S5 [45]).

The PDOS of Ni remains almost the same as in SrNiO_3 , supporting the $d^8\bar{L}^2$ -like electronic structure of Ni, i.e., the change in oxygen stoichiometry mainly affects the ligand hole characteristic of O rather than the valence state of Ni. The

hybridization between the O p_z orbital and Ni e_g orbital near -6 eV in the spin up state has increased on adding the V_O , and this explains how the polarization of O electrons and hence the magnitude of the O moment was reduced. This is the opposite of what is expected for a $\text{SrCoO}_{3-\delta}$ system, where the unoccupied peak of Co is shifted to a higher energy, explained by the ligand hole in e_g [49]. Also, the mechanism for an increase in magnetization is different from that of SrTiO_3 , where an oxygen vacancy leads to a magnetic moment due to the emergence of spin up states in Ti atoms that were formerly $S = 0$ [80].

Two O vacancies in the $2 \times 2 \times 2$ supercell system gives the formula $\text{SrNiO}_{2.75}$ ($\delta = 0.250$). When one vacancy position is fixed, there are seven possible locations for the second one [Fig. 1(a)]. Each configuration is labeled by the crystallographic direction between the two vacancies. Considering spin directions of Ni as well as the vacancy locations for *C*-AFM and *A*-AFM further increases the number of possible configurations. However, we focused on only one configuration for each case based on the results from $\text{SNO}_{2.875}$, because the addition of the first vacancy did not affect the order of energy (FM < *A*-AFM < *C*-AFM < *G*-AFM). Among all possible magnetic ordering and vacancy position configurations, the FM [222] structure illustrated in Fig. 1(b) was the lowest energy state. Other configurations are visualized in Supplemental Material Fig. S6 [45]. All of the AFM configurations were unstable and SNO shows a robust stability in its FM ordering. At $\delta = 0.250$, the net magnetization is about $0.5 \mu_B/\text{f.u.}$ regardless of the vacancy position (Table II), so these results provide a reference for experimentally synthesized SNO in which the oxygen vacancy locations would likely be random. The formation energy of the second oxygen vacancy depends on the configuration. It is higher than the first vacancy on average, but the most stable configuration has a lower formation energy (0.24 eV).

Comparing the one-vacancy and two-vacancy cases, as we add oxygen vacancies, the magnetic moment of Ni increases and the absolute moment of O decreases (Fig. 5). These two effects combine to increase the total magnetization of the system. A similar behavior was empirically observed in NdNiO_3 , where inducing oxygen vacancies increases the saturation magnetization from the canted as-grown state [10]. This was explained not only because of a change in Ni valence state but also due to the overlap between the trapped electrons in the vacancy and Ni *d* orbitals and the formation of a Ni- V_O -Ni complex.

TABLE II. Relative total energies (E), magnetic moment (μ) of Ni and O, total magnetic moment per formula unit (f.u.) of FM SNO $\delta = 0.250$, and the second oxygen vacancy formation energy (ΔE_f) depending on the vacancy configurations. Magnetic moments of Ni and O are averaged over the supercell.

Config.	E (meV/f.u.)	μ of Ni (μ_B)	μ of O (μ_B)	Total $\mu/\text{f.u.}$ (μ_B)	ΔE_f (eV)
[001]	99.14	1.368	-0.284	0.492	1.04
[010]	10.65	1.389	-0.289	0.485	0.33
[011]	13.30	1.371	-0.285	0.490	0.35
[121]	16.76	1.379	-0.287	0.492	0.38
[022]	46.69	1.384	-0.290	0.492	0.63
[220]	57.17	1.366	-0.285	0.488	0.70
[222]	0	1.388	-0.290	0.493	0.24

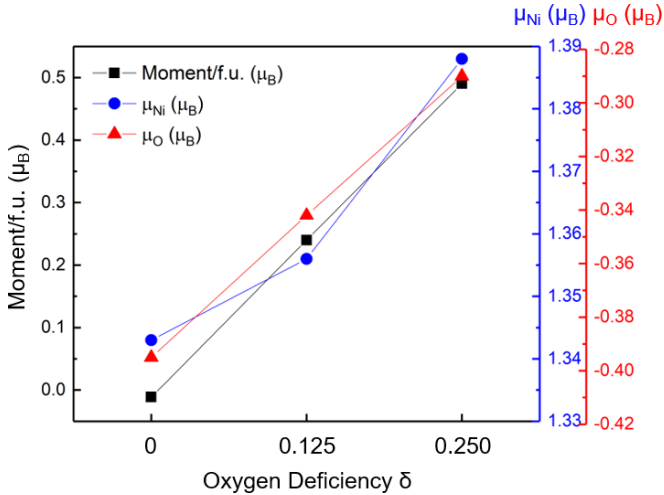


FIG. 5. Total, Ni, and O magnetic moment dependence on δ . $\delta = 0.250$ Ni moments were averaged over all seven FM configurations.

In order to understand the hybridization between Ni and O, the ground state configuration [222] was chosen for the PDOS analysis. Figures 2(c) and 2(d) show the PDOS of Ni in octahedral [Ni(Oct)] or pyramid coordination [Ni(Pyr)], and adjacent O atoms along the c axis. Both octahedra and pyramids are slightly compressed in the z direction by about 5%, so there will be a small energy splitting within the t_{2g} and e_g orbitals. In particular, d_{z^2} will have a higher energy than $d_{x^2-y^2}$, and d_{yz} and d_{zx} will have a higher energy than d_{xy} , however, the grouping of t_{2g} and e_g is maintained. The peak around -3 eV of Ni e_g and O p_z relates to the spin down hybridization between Ni and O. For Ni(Pyr), a peak around -6.5 eV in the spin up states stands out for both Ni e_g and O p_z PDOS in comparison with Ni(Oct). This explains how O(Pyr) ($-0.174 \mu_B$) has a lower magnetic moment than O(Oct) ($-0.388 \mu_B$), and thus the total magnetization increases. The magnetic moment of Ni slightly changed as well, where Ni(Oct) ($1.460 \mu_B$) is higher than Ni(Pyr) ($1.315 \mu_B$). Even though the volume change observed in the direction of the oxygen vacancy is the same, the behavior is different from that of Co in $\text{SrTi}_{0.75}\text{Co}_{0.25}\text{O}_{3-\delta}$, which has a higher magnetic moment when the coordination of oxygen atoms decreases [81].

A similar behavior is observed in the spin polarization as was seen for $\delta = 0.125$. The PDOS for Ni either in Ni(Oct) or Ni(Pyr) are almost unchanged, which could indicate that the excess electrons resulting from the removed O atoms are delocalized [65]. O participating in the octahedral coordination (Ni-O-Ni-O-Ni) has an electronic structure similar to that in nondefective SNO [Fig. 2(a)], and O along the Ni-O-Ni- V_O -Ni direction participating in the pyramid coordination exhibits a distinct ligand hole characteristic from the peak increase above E_F . This trend was not only observed for the [222] configuration, but also observed for other configurations as well. The Bader charge (Table I) of Ni adjacent to V_O is slightly smaller than that of Ni surrounded by six O atoms, which could indicate that the extra electron generated by the removal of one O has a preference to locate near the V_O site, but

because all Ni and O have very small changes in their charge, it would be more plausible that the extra electron delocalizes.

A third oxygen vacancy was added to the supercell, and the results are shown in Supplemental Material Fig. S7 [45]. Because there are more vacancy configurations available with the third one, the third position was selected to keep the distance between the other two vacancies as far as possible, based on the finding for the two-vacancy case that the [222] configuration was the most stable case. The trend in the electronic and magnetic properties upon introducing the third vacancy is similar to the one- and two-vacancy cases: FM ordering remains the most stable and the total magnetization increases due to the increase in Ni moment and decrease in the net O moment. The PDOS of Ni remains nearly the same as the two vacancy case and the PDOS of O depends whether it is in a Ni-O-Ni- V_O -Ni (O1) or a Ni-O-Ni-O-Ni (O2) configuration. The vacancy formation energy with respect to [222] $\text{SNO}_{2.75}$ was 0.80 eV.

Overall, these observations support the model that Ni in SNO_3 has an initial state close to $2+$ with ligand holes on O ($d^8 \underline{L}^2$ mixed with $d^7 \underline{L}$), and the removal of O appears to have more effect on the ligand hole of O than Ni. Observing the trend from $\delta = 0$ to $\delta = 0.375$, the half-metallic property is not affected by the O vacancy; however, the states in the conduction band mainly originate from the electrons of oxygens participating in the π bonding. Moreover, the covalency of the Ni-O bond decreases as oxygen vacancy concentration increases.

C. Extension to other $A^{2+}\text{NiO}_3$ systems

In order to generalize the unusual behavior of SNO to perovskite ANiO_3 with other divalent A cations, we performed an analogous analysis on CaNiO_3 (CNO) and BaNiO_3 (BNO). Ca and Ba were chosen because they are one period lower or higher than Sr. Table III shows a summary of the structure, electronic, and magnetic properties of ANiO_3 . All of them were metallic and stable in the ferromagnetic configuration. Both the magnetic moment of Ni and the magnitude of the moment of O increases as the ionic radius of A^{2+} increases. The magnetic behavior of Ni and O in CNO and BNO were both analogous to that of SNO; Ni is antiferromagnetically coupled with O, which has a substantial moment, and as a result the net magnetization is negligible. This similarity also appears in the PDOS of Ni and O shown in Figs. 2(e) and 2(f). The occupancy of t_{2g} and e_g are the same, in which e_g is spin polarized whereas t_{2g} is not. Moreover, the ligand hole feature in the O p orbital with σ bonding appears distinctly in all three cases. These results give an interesting insight into nickelate compounds, suggesting that oxides with higher formal valence Ni include O ligand holes instead of Ni $3+$ or $4+$. We expect these characteristics will appear not only in perovskite ANiO_3 but also in 4H hexagonal ANiO_3 based on the similarity between perovskite SNO and 4H SNO [35].

To compare the structural stability among ANiO_3 , we consider the predictions of the tolerance factor. The Goldschmidt tolerance factor t is given by

$$t = \frac{r_A + r_O}{\sqrt{2}(r_{Ni} + r_O)},$$

TABLE III. Shannon ionic radius (r), tolerance factors, $E_{\text{cubic}} - E_{\text{hexagonal}}$ per formula unit ($\Delta E/\text{f.u.}$), electronic and magnetic properties of $A^{2+}\text{NiO}_3$ ($A = \text{Ca, Sr, Ba}$).

A	r (pm)	t	τ	$\Delta E/\text{f.u.}$ (meV)	Electronic property	Magnetic ordering	μ of A (μ_B)	μ of Ni (μ_B)	μ of O (μ_B)
Ca	100	0.903	4.594	344.06	Half metallic	FM	0.024	1.208	-0.360
Sr	118	0.970	4.383	384.72	Half metallic	FM	0.011	1.343	-0.395
Ba	135	1.034	4.356	864.50	Metallic	FM	0.007	1.528	-0.437

where r_i represents the ionic radius of ion i , and the perovskite structure is expected for $0.9 < t < 1$. A more recently defined tolerance factor τ is given by [82]

$$\tau = \frac{r_{\text{O}}}{r_{\text{Ni}}} - n_A \left(n_A - \frac{\frac{r_A}{r_{\text{Ni}}}}{\ln\left(\frac{r_A}{r_{\text{Ni}}}\right)} \right),$$

where n_A is the oxidation state of the A cation, which is fixed to 2 in this case. The criterion for the perovskite structure to form is $\tau < 4.18$. Table III contains the tolerance factors calculated using the Shannon ionic radii of Ca^{2+} , Sr^{2+} , Ba^{2+} , Ni^{4+} , and O^{2-} . According to t , the perovskite structure is more likely to form for CNO than for SNO or BNO due to the lower ionic radius of Ca^{2+} , but experimentally, other factors such as epitaxial strain can be used to stabilize perovskite structures despite their tolerance factors predicting that other structures are favored. This trend is opposite for τ , which arises from the fact that t decreases with decreasing r_A whereas τ increases with decreasing r_A . In order to clarify this discrepancy, we compared the energy difference between cubic and hexagonal structures, ΔE , defined as (energy of cubic $A^{2+}\text{NiO}_3$ per f.u.) - (energy of hexagonal $A^{2+}\text{NiO}_3$ per f.u.) for nondefective structures. The results in Table III indicate that the energy difference becomes smaller for Ca^{2+} , which is consistent with the trend in the Goldschmidt tolerance factor. Although the applicability of tolerance factors in compounds with strong covalent character remains questionable, both t and τ will be lowered towards the perovskite regime when O has a ligand hole character and as a consequence r_{O} decreases.

IV. CONCLUSIONS

We used DFT to predict the electronic and magnetic properties of stoichiometric and oxygen-deficient cubic perovskite $\text{SrNiO}_{3-\delta}$. The results are consistent with the presence of ligand holes and Ni cations exhibiting a mixture of $d^8\bar{L}^2$ and $d^7\bar{L}$ states with a high contribution of $d^8\bar{L}^2$. Ferromagnetism

mediated by O and half metallicity are robust for SNO with $\delta = 0, 0.125, \text{ and } 0.250$ or for epitaxially strained SNO with $\delta = 0$. In particular, for $\delta = 0.250$, the magnetic ordering is little affected by the vacancy positions. Although Ni is ferromagnetically ordered, because of the antiferromagnetic coupling between Ni and O and the magnetic moment of the O due to its ligand holes, the total magnetization of the system is nearly zero at $\delta = 0$. However, the magnetism increases as SNO becomes oxygen deficient, corresponding to the removal of the O moment, and the hybridization between Ni and O becomes weaker as an oxygen vacancy is introduced. Other $A^{2+}\text{NiO}_3$ compounds, CaNiO_3 and BaNiO_3 , show analogous behavior.

SNO itself has proven to be challenging to synthesize with a cubic perovskite structure, and a hexagonal structure typically forms instead of the cubic. However, a smaller divalent cation as in CaNiO_3 reduces the Goldschmidt tolerance factor towards the perovskite regime and may be easier to synthesize. Moreover, cubic SNO in a heterostructure has a possibility to be stabilized over hexagonal SNO without losing its properties. Some of the computational results for 4H hexagonal SNO, including the FM configuration of the Ni, the half metallicity, and the PDOS of Ni and O, are analogous to those found in our study of cubic SNO. This work demonstrates the importance of ligand holes in oxides with formally high valence Ni, and motivates further growth studies and characterization of the electronic and magnetic properties of nickelates with divalent A -site cations.

ACKNOWLEDGMENTS

This work was supported by the NSF MRSEC program under Award No. DMR 1419807. C.A.R. acknowledges support of SMART, an nCore Center of the Semiconductor Research Corporation. J.L. and R.C. were supported by the Air Force Office of Scientific Research Young Investigator Program under Grant No. FA9550-19-1-0063.

-
- [1] S. Middey, J. Chakhalian, P. Mahadevan, J. W. Freeland, A. J. Millis, and D. D. Sarma, *Annu. Rev. Mater. Res.* **46**, 305 (2016).
- [2] S. J. Catalano, M. Gilbert, J. Fowlie, J. Iniguez, J.-M. Triscone, and J. Kreisel, *Rep. Prog. Phys.* **81**, 046501 (2018).
- [3] T. Mizokawa, A. Fujimori, T. Arima, Y. Tokura, N. Mori, and J. Akimitsu, *Phys. Rev. B* **52**, 13865 (1995).
- [4] M. N. Grisolia, J. Varignon, G. Sanchez-Santolino, A. Arora, S. Valencia, M. Varela, R. Abrudan, E. Weschke, E. Schierle, J. E. Rault *et al.*, *Nat. Phys.* **12**, 484 (2016).
- [5] J. A. Alonso, J. L. García-Muñoz, M. T. Fernández-Díaz, M. A. G. Aranda, M. J. Martínez-Lope, and M. T. Casais, *Phys. Rev. Lett.* **82**, 3871 (1999).
- [6] M. T. Fernández-Díaz, J. A. Alonso, M. J. Martínez-Lope, M. T. Casais, and J. L. García-Muñoz, *Phys. Rev. B* **64**, 144417 (2001).
- [7] M. Hepting, R. J. Green, Z. Zhong, M. Bluschke, Y. E. Suyolcu, S. Macke, A. Frano, S. Catalano, M. Gibert, R. Sutarto *et al.*, *Nat. Phys.* **14**, 1097 (2018).
- [8] H. Park, A. J. Millis, and C. A. Marianetti, *Phys. Rev. Lett.* **109**, 156402 (2012).

- [9] M. Kotiuga, Z. Zhang, J. Li, F. Rodolakis, H. Zhou, R. Sutarto, F. He, Q. Wang, Y. Sun, Y. Wang *et al.*, *Proc. Natl. Acad. Sci. USA* **116**, 21992 (2019).
- [10] L. Wang, S. Dash, L. Chang, L. You, Y. Feng, X. He, K. Jin, Y. Zhou, H. G. Ong, P. Ren *et al.*, *ACS Appl. Mater. Interfaces* **8**, 9769 (2016).
- [11] S. Johnston, A. Mukherjee, I. Elfimov, M. Berciu, and G. A. Sawatzky, *Phys. Rev. Lett.* **112**, 106404 (2014).
- [12] G. Coslovich, B. Huber, W.-S. Lee, Y.-D. Chuang, Y. Zhu, T. Sasagawa, Z. Hussain, H. A. Bechtel, M. C. Martin, Z.-X. Shen *et al.*, *Nat. Commun.* **4**, 2643 (2013).
- [13] B.-X. Wang, H. Zheng, E. Kriviyakina, O. Chmaissem, P. P. Lopes, J. W. Lynn, L. C. Gallington, Y. Ren, S. Rosenkranz, J. F. Mitchell, and D. Phelan, *Phys. Rev. Mater.* **4**, 084409 (2020).
- [14] D. Li, B. Y. Wang, K. Lee, S. P. Harvey, M. Osada, B. H. Goodge, L. F. Kourkoutis, and H. Y. Hwang, *Phys. Rev. Lett.* **125**, 027001 (2020).
- [15] M. Osada, B. Y. Wang, B. H. Goodge, K. Lee, H. Yoon, K. Sakuma, D. Li, M. Miura, L. F. Kourkoutis, and H. Y. Hwang, *Nano Lett.* **20**, 5735 (2020).
- [16] K. S. Nanjundaswamy, A. Lewicki, Z. Kakol, P. Gopalan, P. Metcalf, J. M. Honig, C. N. R. Rao, and J. Spalek, *Phys. C (Amsterdam, Neth.)* **166**, 361 (1990).
- [17] E. Ksepko, *Int. J. Hydrogen Energy* **39**, 8126 (2014).
- [18] Y. Takeda, T. Hashino, H. Miyamoto, F. Kanamaru, S. Kume, and M. Koizumi, *J. Inorg. Nucl. Chem.* **34**, 1599 (1972).
- [19] J. J. Lander and L. A. Wooten, *J. Am. Chem. Soc.* **73**, 2452 (1951).
- [20] H. Shibahara, *J. Solid State Chem.* **69**, 81 (1987).
- [21] J. G. Lee, H. J. Hwang, O. Kwon, O. S. Jeon, J. Jang, and Y. G. Shul, *Chem. Commun.* **52**, 10731 (2016).
- [22] R. Gottschall, R. Schöllhorn, M. Muhler, N. Jansen, D. Walcher, and P. Gütllich, *Inorg. Chem.* **37**, 1513 (1998).
- [23] M. Zinkevich, *J. Solid State Chem.* **178**, 2818 (2005).
- [24] J. Lee and G. F. Holland, *J. Solid State Chem.* **93**, 267 (1991).
- [25] F. Abraham, S. Minaud, and C. Renard, *J. Mater. Chem.* **4**, 1763 (1994).
- [26] M. Bianchini, A. Schiele, S. Schweidler, S. Siculo, F. Fauth, E. Suard, S. Indris, A. Mazilkin, P. Nagel, S. Schuppler *et al.*, *Chem. Mater.* **3**, 9211 (2020).
- [27] V. W. Bronger, H. Bade, and W. Klemm, *Z. Anorg. Allg. Chem.* **333**, 188 (1964).
- [28] A. N. Mansour, C. A. Melendres, M. Pankuch, and R. A. Brizzolara, *J. Electrochem. Soc.* **141**, L69 (1994).
- [29] A. N. Mansour, and C. A. Melendres, *J. Phys. Chem. A* **102**, 65 (1998).
- [30] H. Seki, Y. Hosaka, T. Saito, M. Mizumaki, and Y. Shimakawa, *Angew. Chem. Int. Ed.* **55**, 1360 (2016).
- [31] H. Seki, T. Saito, and Y. Shimakawa, *J. Jpn. Soc. Powder Powder Metall.* **63**, 609 (2016).
- [32] L. Wang, Z. Yang, M. E. Bowden, J. W. Freeland, P. V. Sushko, S. R. Spurgeon, B. Matthews, W. S. Samarakoon, H. Zhou, Z. Feng *et al.*, *Adv. Mater.* **32**, 2005003 (2020).
- [33] L. Wang, Z. Yang, X. Yin, S. D. Taylor, X. He, C. S. Tang, M. E. Bowden, J. Zhao, J. Wang, J. Liu *et al.*, *Sci. Adv.* **7**, eabe2866 (2021).
- [34] G. Chen, C. Dai, and C. Ma, in *Proceedings of the 2014 International Conference on Mechatronics, Electronic, Industrial and Control Engineering*, edited by L. Chang, C. Guiran, and L. Zhen (Atlantis, Shenyang, China, 2014), Vol. 5, pp. 746–749.
- [35] G. Y. Chen, C. L. Ma, D. Chen, and Y. Zhu, *J. Solid State Chem.* **233**, 438 (2016).
- [36] S. Mehmood, Z. Ali, I. Khan, and I. Ahmad, *J. Electron. Mater.* **49**, 3780 (2020).
- [37] F. Fan, Z. Li, Z. Zhao, K. Yang, and H. Wu, *Phys. Rev. B* **94**, 214401 (2016).
- [38] S. L. Dudarev, G. A. Botton, S. Y. Savrasov, C. J. Humphreys, and A. P. Sutton, *Phys. Rev. B* **57**, 1505 (1998).
- [39] H. J. Monkhorst and J. D. Pack, *Phys. Rev. B* **13**, 5188 (1976).
- [40] Y. Takeda, F. Kanamura, M. Shimada, and M. Koizumi, *Acta Crystallogr.* **32**, 2464 (1976).
- [41] R. N. Song, M. H. Hu, X. R. Chen, and J. D. Guo, *Front. Phys.* **10**, 106802 (2015).
- [42] K. Momma and F. Izumi, *J. Appl. Crystallogr.* **44**, 1272 (2011).
- [43] M. Yu and D. R. Trinkle, *J. Chem. Phys.* **134**, 064111 (2011).
- [44] L. Wang, T. Maxisch, and G. Ceder, *Phys. Rev. B* **73**, 195107 (2006).
- [45] See Supplemental Material at <http://link.aps.org/supplemental/10.1103/PhysRevMaterials.5.094413> for HSE results, hexagonal structure and properties, total DOS, slab structure and properties, PDOS of O on all x , y , and z directions of Ni in SrNiO_{2.875}, visualization of possible configurations of SrNiO_{2.75}, calculation results of SrNiO_{2.625}, properties of SrNiO₃ and SrNiO_{2.875}, and PDOS integration.
- [46] J. Varignon, M. N. Grisolia, J. Íñiguez, A. Barthélémy, and M. Bibes, *npj Quantum Mater.* **2**, 21 (2017).
- [47] G. M. Dalpian, Q. Liu, J. Varignon, M. Bibes, and A. Zunger, *Phys. Rev. B* **98**, 075135 (2018).
- [48] A. Mercy, J. Bieder, J. Íñiguez, and P. Ghosez, *Nat. Commun.* **8**, 1677 (2017).
- [49] J. Lim and J. Yu, *Phys. Rev. B* **98**, 085106 (2018).
- [50] A. Hampel and C. Ederer, *Phys. Rev. B* **96**, 165130 (2017).
- [51] V. Bisogni, S. Catalano, R. J. Green, M. Gibert, R. Scherwitzl, Y. Huang, V. N. Strocov, P. Zubko, S. Balandeh, J.-M. Triscone *et al.*, *Nat. Commun.* **7**, 13017 (2016).
- [52] S. R. Barman, A. Chainani, and D. D. Sarma, *Phys. Rev. B* **49**, 8475 (1994).
- [53] T. Mizokawa, D. Khomskii, and G. A. Sawatzky, *Phys. Rev. B* **61**, 11263 (2000).
- [54] P. C. Rogge, R. U. Chandrasena, A. Cammarata, R. J. Green, P. Shafer, B. M. Lefler, A. Huon, A. Arab, E. Arenholz, H. N. Lee *et al.*, *Phys. Rev. Mater.* **2**, 015002 (2018).
- [55] S. Mathi Jaya, R. Jagadish, R. S. Rao, and R. Asokamani, *Phys. Rev. B* **43**, 13274 (1991).
- [56] C. Lan, H. Li, and S. Zhao, *J. Comput. Electron.* **19**, 905 (2020).
- [57] R. Li, D. Xin, S. Huang, Z. Wang, L. Huang, and X. Zhou, *Chin. J. Phys.* **56**, 2829 (2018).
- [58] H. Chen and J. H. Harding, *Phys. Rev. B* **85**, 115127 (2012).
- [59] M. L. Medarde, *J. Phys.: Condens. Matter* **9**, 1679 (1997).
- [60] B. Geisler and R. Pentcheva, *Phys. Rev. B* **102**, 020502(R) (2020).
- [61] J. R. Petrie, C. Mitra, H. Jeon, W. S. Choi, T. L. Meyer, F. A. Reboredo, J. W. Freeland, G. Eres, and H. N. Lee, *Adv. Funct. Mater.* **26**, 1564 (2016).
- [62] P. Walke, S. Gupta, Q. R. Li, M. Major, W. Donner, B. Mercey, and U. Lüders, *J. Phys. Chem. Solids* **123**, 1 (2018).
- [63] H. Jeon, W. S. Choi, J. W. Freeland, H. Ohta, C. U. Jung, and H. N. Lee, *Adv. Mater.* **25**, 3651 (2013).

- [64] A. Khare, D. Shin, T. S. Yoo, M. Kim, T. D. Kang, J. Lee, S. Roh, I.-H. Jung, J. Hwang, S. W. Kim *et al.*, *Adv. Mater.* **29**, 1606566 (2017).
- [65] R. Merkle, Y. A. Mastrikov, E. A. Kotomin, M. M. Kuklja, and J. Maier, *J. Electrochem. Soc.* **159**, B219 (2011).
- [66] M. Hoffmann, V. S. Borisov, S. Ostanin, I. Mertig, W. Hergert, and A. Ernst, *Phys. Rev. B* **92**, 094427 (2015).
- [67] T. Yokota, S. Kito, S. Murata, and M. Gomi, *Vacuum* **84**, 663 (2009).
- [68] R. K. Hona and F. Ramezanipour, *Polyhedron* **167**, 69 (2019).
- [69] L. Suescun, O. Chmaissem, J. Mais, B. Dabrowski, and J. D. Jorgensen, *J. Solid State Chem* **180**, 1698 (2007).
- [70] Q. Ji, L. Bi, J. Zhang, H. Cao, and X. S. Zhao, *Energy Environ. Sci.* **13**, 1408 (2020).
- [71] T. Das, J. D. Nicholas, and Y. Qi, *Phys. Chem. Chem. Phys.* **22**, 9723 (2020).
- [72] C. Zhang and P. D. Bristowe, *RSC Adv.* **3**, 12267 (2013).
- [73] M. T. Curnan and J. R. Kitchin, *J. Phys. Chem. C* **118**, 28776 (2014).
- [74] A. A. Emery and C. Wolverton, *Sci. Data* **4**, 170153 (2017).
- [75] H. Y. Su and K. Sun, *J. Mater. Sci.* **50**, 1701 (2015).
- [76] T. Das, J. D. Nicholas, and Y. Qi, *ECS Trans.* **78**, 2807 (2017).
- [77] T. Das, J. D. Nicholas, and Y. Qi, *J. Mater. Chem. A* **5**, 25031 (2017).
- [78] B. Raveau and M. M. Seikh, *Cobalt Oxides: From Crystal Chemistry to Physics* (Wiley-VCH, Weinheim, 2012).
- [79] L. Zhang, B. Liu, H. Zhuang, P. R. C. Kent, V. R. Cooper, P. Ganesh, and H. Xu, *Comput. Mater. Sci.* **118**, 309 (2016).
- [80] Y. Zhang, J. Wang, M. P. K. Sahoo, T. Shimada, and T. Kitamura, *Phys. Chem. Chem. Phys.* **17**, 27136 (2015).
- [81] J. M. Florez, S. P. Ong, M. C. Onbasli, G. F. Dionne, P. Vargas, G. Ceder, and C. A. Ross, *Appl. Phys. Lett.* **100**, 252904 (2012).
- [82] C. J. Bartel, C. Sutton, B. R. Goldsmith, R. Ouyang, C. B. Musgrave, L. M. Ghiringhelli, and M. Scheffler, *Sci. Adv.* **5**, eaav0693 (2019).